The Complete In-Gap Electronic Structure of Colloidal Quantum Dot Solids and Its Correlation with Electronic Transport and Photovoltaic Performance

*Khabiboulakh Katsiev, Alexander H. Ip, Armin Fischer, Iori Tanabe, Xin Zhang, Ahmad R. Kirmani, Oleksandr Voznyy, Lisa R. Rollny, Kang Wei Chou, Susanna M. Thon, Graham H. Carey, Xiaoyu Cui, Aram Amassian, Peter Dowben, Edward H. Sargent, and Osman M. Bakr**

Solar cells based on colloidal quantum dot (CQD) solids have attracted tremendous interest due to the ease of preparation from solution and tunability of the nanocrystal size.[1,2] This means excellent sample control, low cost, and large area fabrication compatible with roll-to-roll methods based on flexible substrates. The quantum size effect allows the bandgap of CQDs to be tailored to specific applications, such as multi-junction solar cells that absorb across the broad solar spectrum, including a significant portion in the infrared.[3]

Recently, CQD solar cells, using metal halide passivation, were reported that achieved a certified power conversion efficiency of 7.0%, a record for this class of materials.[4] The nanometer-diameter CQDs exhibit a high surface area-to-volume ratio, making proper management of surface states very important, since trap states associated with surface defects are the key factor limiting CQD photovoltaic device performance today:[4,5] unpassivated sites give rise to surface defect-related electronic trap states within the bandgap that create fast non-radiative de-excitation channels for photogenerated charge carriers. The geometric structure and dimensions of organic ligands were found to prevent the ligands from fully complexing to all surface cation sites in need of passivation, particularly hard-to-access sites such as inter-cation trenches.[4] In contrast, atomic ligands such as halides are sufficiently compact to infiltrate and passivate otherwise inaccessible sites.

Thorough investigation of the electronic character of CQD solids is of great importance to achieving further improvements in performance through identification and elimination of detrimental trap states within the bandgap. Much progress has been made in this direction,[5–10] including the use of photovoltage transient measurements to explore the midgap density of states in CQD solids as a function of the metal halide passivation schemes employed.[4,11] However, this technique probes only the portion of the bandgap between the two quasi-Fermi levels. In fact, electronic transport is influenced instead by those traps lying beneath the hole quasi-Fermi level, and lying above the electron quasi-Fermi level. Furthermore, optical techniques have been used to measure midgap states;[12,13] however, parity selection rules may complicate interpretation of optical measurements and therefore may not provide a complete picture. For these reasons, a direct measurement of the entire band structure of PbS quantum dot solids – one that would resolve in detail the entire region from the conduction band to the valence band, elucidating the impact of surface passivation on both deep and shallow states within the gap is of urgent interest.

Direct techniques for probing electronic structure, principally photoelectron spectroscopies (PES) and scanning tunneling spectroscopy (STS), have greatly aided in the understanding of the fundamental properties of various materials systems including in heterogeneous catalysts,[14] solid oxide fuel cells,[15] and nanocrystals and nanocrystal films.[16–19] Previous photovoltaics-relevant work includes studies on prototypical polymer/fullerene hybrid solar cells,[20] organic photovoltaic materials,[21] thin film solar cell interfaces,[22] and metal oxides used for charge extraction.[23,24] PES techniques provide a statistically robust picture of the electronic structure as it relates to macroscopic device performance, since they deliberately probe over macroscopic areas, whereas STS is a local probe technique allowing the electronic structure to be probed on the nanometer scale. Spectroscopies can be combined to obtain a picture of the entire electronic structure, where PES will offer valence band associated states,[25] and inverse photoelectron spectroscopy (IPES) can report on largely unfilled states such as those in the conduction band.

Dr. K. Katsiev, A. R. Kirmani, Dr. K. W. Chou, Prof. A. Amassian, Prof. O. M. Bakr
Division of Physical Sciences and Engineering
Solar and Photovoltaic Engineering Center
King Abdullah University of Science and Technology (KAUST)
Thuwal, 23955–6900, Saudi Arabia
E-mail: Osman.Bakr@kaust.edu.sa

A. H. Ip, Dr. A. Fischer, Dr. O. Voznyy, L. R. Rollny, Dr. S. M. Thon,[+] G. H. Carey, Prof. E. H. Sargent
Department of Electrical and Computer Engineering
University of Toronto
Toronto, Ontario, M5S 3G4, Canada

I. Tanabe, X. Zhang, Prof. P. Dowben
Department of Physics and Astronomy
Jorgensen Hall, 855 North 16th Street
University of Nebraska-Lincoln
Lincoln, NE, 68588–0299, USA

Dr. X. Y. Cui
Canadian Light Source
Saskatoon, SK, S7N 2V3, Canada

[+]Present address: Department of Electrical and Computer Engineering, Johns Hopkins University, Baltimore, Maryland 21218, USA

DOI: 10.1002/adma.201304166

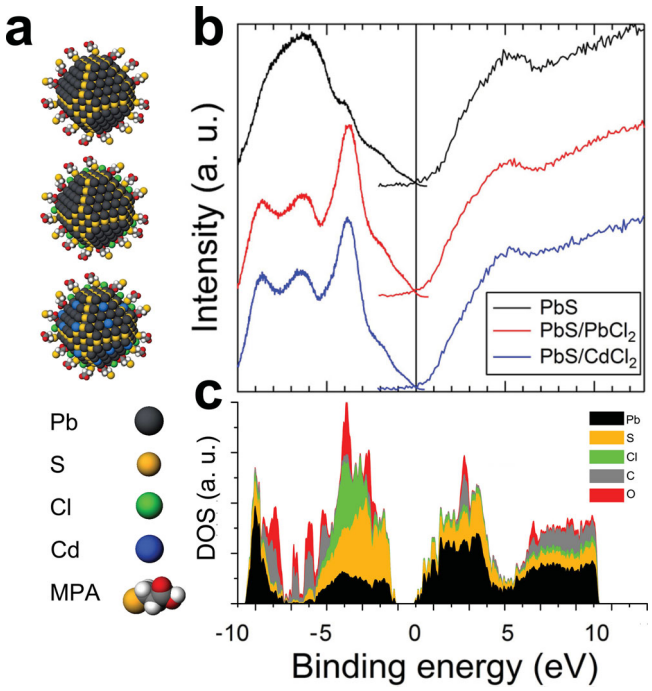

Figure 1. a) Schematic representations of PbS CQDs with various passivation schemes: MPA only (top), $PbCl_2$ passivation (middle) and $CdCl_2$ passivation (bottom). Note that the MPA and Cl ligands are only shown around the periphery for clarity, but they do exist over the whole surface. b) PES (left, showing valence band structures) and IPES (right, showing conduction band structures) spectra of PbS CQD films with different passivation schemes corresponding with the diagrams in part (a). c) DFT calculated density of states for a 2.4 nm PbS CQD passivated with MPA and Cl ligands. The colors show the contribution from each element.

Here, we combine synchrotron-based PES and inverse photoemission spectroscopy (IPES) to measure directly the electronic structure of the entire valence and conduction bands of PbS CQD films. We also deploy density functional calculations that both validate and help to explain the observed features in the electronic spectra. Specifically, we report the structure of the valence and conduction bands of PbS CQD films formed using mercaptopropionic acid (MPA) as a ligand that is utilized to build photovoltaic devices.[26] We examine the effect of metal halide passivation on the PbS CQD film occupied and unoccupied electronic structure by additionally studying films of CQDs that have been passivated with $CdCl_2$ or $PbCl_2$ during synthesis. We find that trap states are indeed affected by the passivation scheme used, as suggested by recent computational and charge transport studies.[8,11] We find that halide ligands reduce deep trap states, and we find from IPES that the nature of the metal cation at the CQD surface determines the shallow trap state density near the conduction band edge. We relate these findings to device properties by measuring the electron mobility in the various samples: we observe improved electron mobility when the density of shallow conduction band-associated trap states is decreased with the aid of the best cation. Finally, we show that the PES-measured reductions in midgap and shallow trap states due to metal halide passivation ultimately result in improved photovoltaic device efficiency.

Complete electronic structures of MPA- and hybrid-passivated PbS CQD films obtained by a combination of PES and IPES are shown in **Figure 1**, accompanied by schematic representations of the corresponding quantum dots (Figure 1a). As seen in Figure 1b, a broad feature exists deep in the valence band of the PbS-MPA-only sample. In contrast, both halide passivated samples show significant changes in the structure, with spectral features at 1.8, 3.8, 6.4 and 8.5 eV becoming more pronounced with narrowed energy width, closely resembling the detailed valence band structure of single crystal PbS samples, where for the spectra acquired at the same photon energy of ca. 27 eV similar spectral features at 1.7, 3.3, and 5.5 eV have been observed.[27,28] The broad feature of the PbS-MPA-only sample may be due to excess carbon from organic ligands, as previously measured by XPS,[4] and in agreement with literature reports.[29,30] During the metal halide passivation step, a fraction of long-chain oleic acid ligands are displaced which results in the suppression of carbon signals seen here. To validate further these assignments, we calculated the density of states (DOS) obtained using density functional theory for a PbS CQD capped with MPA and Cl (Figure 1c). The broad feature is aligned with carbon and oxygen related peaks. Chlorine is found to have a large contribution in the valence band, explaining the prominence of the 3.8 eV feature in the halide-passivated samples.

The relevant region of interest for the operation of photovoltaic devices comprises the region of the bandgap and the band edges where charge transport and trapping occur. Therefore, in **Figure 2** we focus on the changes in the valence band edge (Figure 2a) and the conduction band edge (Figure 2b) caused by different passivation schemes.

Investigation of the PES-derived spectra (Figure 2a) shows a significant change associated with the halide passivation. The density of states at the Fermi level is appreciably reduced compared with the PbS-MPA-only film, demonstrating the role of surface halides in reducing deep trap states. To exclude the influence of the tails of the broad carbon and oxygen peaks in the –5 eV to –8 eV region, and show the absolute reduction in the presence of trap states, the multiple peaks were fitted in the PES and IPES spectra (Figure S1 and S2 in the Supporting Information, respectively). The deeper lying spectral features were subtracted, leaving the features attributed to the trap states (Figure S3, Supporting Information), followed by the integration of the residuals (Figure 2d).

Notably, the valence band edge states do not change appreciably between $PbCl_2$ and $CdCl_2$ treated CQDs. We have also observed changes in the absorption spectra of the CQDs following metal halide passivation (Figure S4, Supporting Information), with an improved excitonic peak sharpness. The cause of this is unclear at the moment, but we speculate it is passivation-related rather than due to improved monodispersity.

As seen in Figure 2b, there is a slight shift of the conduction band edge towards the Fermi level for both of the halide passivated samples compared to MPA-only passivation. This is consistent with the view that chlorine can protect the surface from oxidation,[31] with oxygen acting as a p-type dopant.[32,33] Previously, it was shown that there are not substantial enough changes in doping to explain the improvement in device performance.[4] More striking is the marked difference in the tail states at the conduction band edge, measured by integrating

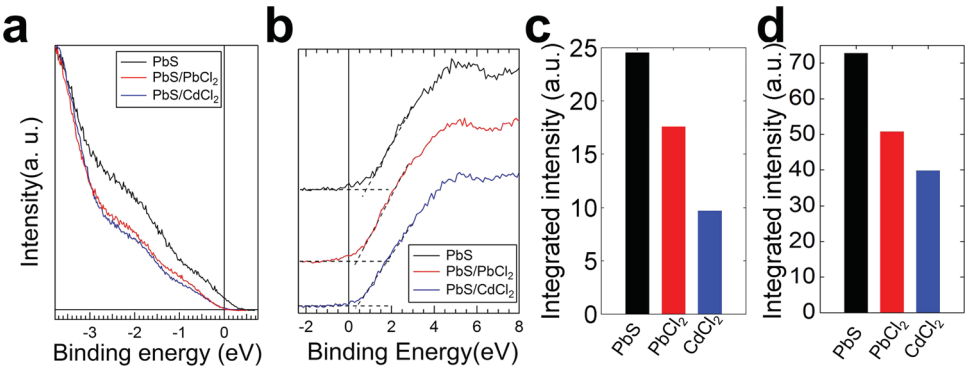

Figure 2. a) Magnified view of the valence band edge as measured by PES. Halide passivation reduces the density of band edge and midgap states, but there is no significant difference between the $PbCl_2$ and $CdCl_2$ treated samples. b) Magnified view of the conduction band edge as measured by IPES with the spectra offset for clarity. The density of states in the band edge tail is reduced by halide passivation and further reduced upon cadmium incorporation. c) Integrated intensity of tail states in (b), in the area bounded by the curve and the dotted lines. d) Integrated intensity of tail states in (a), in the area bounded by the residuals in Figure S3 in the Supporting Information.

the measured PES signal beyond the band edge (Figure 2c). In the PbS-MPA-only sample, a large tail persists past the band edge, which prevents efficient splitting of quasi-Fermi levels because photo-generated charges are consumed in filling of these states, leading to sub-optimal open-circuit voltage (V_{OC}). In comparison, the relative density of states for the $CdCl_2$ passivated sample is dramatically reduced to just 40% compared to the PbS-MPA-only sample; however, this effect is less prominent with the $PbCl_2$ treatment, with a reduction to 70% relative to the PbS sample.

This finding suggests that while the halide ligands are efficient at passivating deep traps, the nature of the cations on the quantum dot surface is crucial for the reduction of shallow traps. This is in agreement with previous work demonstrating changes in device performance based on the incorporation of a wide range of different metal cations at quantum dot surfaces.[11] In that case, density functional theory was used to show that Pb atoms with dangling bonds – likely to occur on surfaces – are likely to form shallow trap states at the conduction band edge. However, certain metal atoms, such as Cd, demonstrated bond adaptability in which states related to undercoordinated surface atoms were formed within the conduction band rather than encroaching on the bandgap. The computational studies predicted that proper cation choice would lead to elimination of shallow traps that would be formed by undercoordination of the surface Pb atoms. However, a direct experimental probe of conduction band edge states has not been presented. Here, the IPES spectra clearly show that Cd prevents formation of shallow, surface-associated trap states that arise from Pb termination of the CQDs. We note that these measurements probe ensemble characteristics of the CQD film and therefore, states with much lower populations may not be visible. These may include localized small bandgap inclusions – due to larger diameter quantum dots – that could also act as efficient recombination centres.[5] However, the ensemble characteristics are useful for examining the effect of passivation on similarly monodisperse populations of CQDs.

To relate these fundamental measurements of the electronic structure of CQD solids with device performance, we built depleted-heterojunction solar cells[4,26] employing the three different classes of CQDs studied above. The device structure consists of a fluorine-doped tin oxide bottom electrode, a TiO_2 n-type electron extracting layer, a CQD film approximately 300 nm in thickness, and a top electrode of MoO_3/Au/Ag.

We studied the electronic transport in these devices using the photocurrent transient method.[34] By measuring the transit time – the time for photocurrent to decay to $1/e$ of its maximum value – across a range of applied biases, we were able to probe the mobility of the limiting charge carrier.

Figure 3a shows the fit of transit time as a function of bias for each sample. As expected, the mobilities for the halide passivated samples are both improved over the solely MPA passivated sample, as shown in Figure 3b. The PbS-MPA-only sample exhibited a mobility of 7.2×10^{-4} cm^2 V^{-1} s^{-1}, while the addition of chloride through $PbCl_2$ resulted in a doubling of the mobility to 1.4×10^{-3} cm^2 V^{-1} s^{-1}. The $CdCl_2$ treated film also shows a modest improvement over the $PbCl_2$ film, with a measured mobility of 1.9×10^{-3} cm^2 V^{-1} s^{-1}. This trend in mobility would be expected to arise from a reduction in transport inhibiting shallow trap states, as was seen in the IPES results. This implies that minority carrier mobility is indeed the limiting mobility in this type of device and that electrons are the probed carriers in photocurrent transient measurements on the films measured herein and in previous reports.[11]

The mobility in CQD films is also affected by interparticle spacing.[35] We therefore investigated as to whether the nanoparticle spacing could be playing a role in the findings on transport. Synchrotron-based grazing-incidence small-angle X-ray scattering (GISAXS) has been used to determine the average centre-to-centre distance of nanocrystal films.[4,36,37] We measured a representative film for each passivation method and found, as shown in Figure 3b and 3c, that the average spacing was approximately the same for all MPA treated films, regardless of chloride or cadmium incorporation. Both halide treated films were found to have a spacing of 3.2 ± 0.2 nm, while the PbS-MPA-only sample had a spacing of 3.0 ± 0.1 nm, equal within error from these measurements. Even though the average interparticle distance in Figure 3c appears slightly

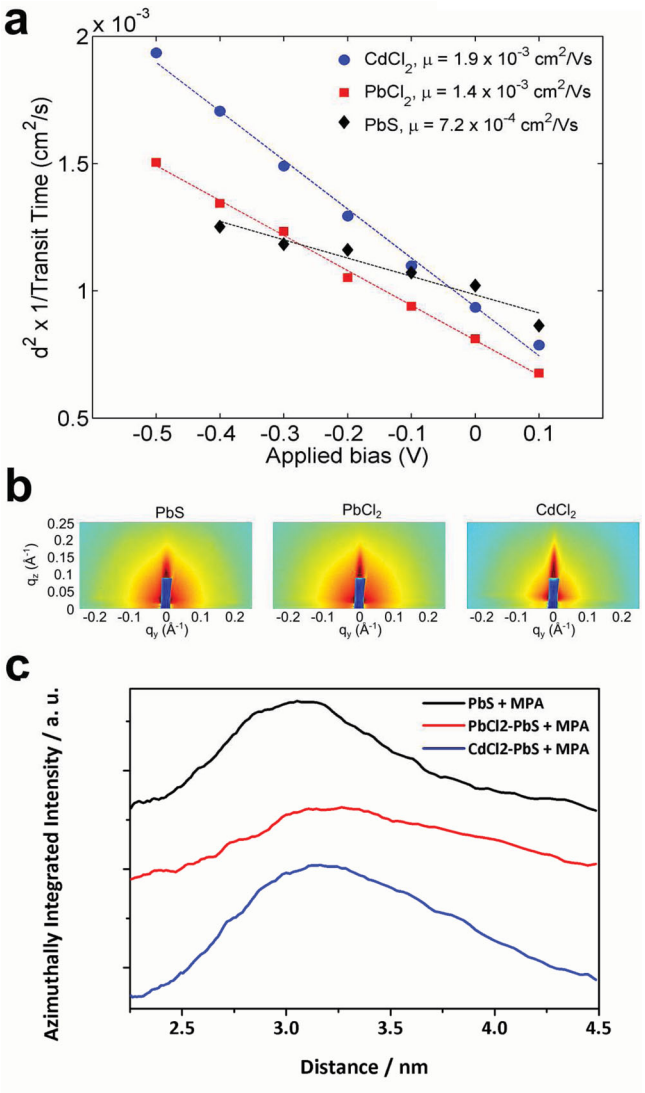

Figure 3. a) The square of film thickness, *d*, divided by photocurrent transient derived transit times as a function of bias. The linear fit is used to calculate the limiting mobility of each film, as shown in the legend. b) GISAXS patterns of MPA-exchanged quantum dot films with different surface passivants. c) Azimuthally integrated GISAXS intensities give the average particle spacing; the average spacings are found to be the same for all passivation schemes in this study. The spectra are offset for clarity; differences in the peak definition are due to slight differences in the sample alignment.

smaller for the PbS-MPA-only sample, this would be expected to improve coupling and boost the measured mobility. However, the metal halide samples still show much improved transport. From this we conclude that the differences in mobility among the different samples are attributable principally to differences in electronic structure resulting from the different surface passivation and not the interparticle spacing.

The performance of solar cells using these films was also evaluated and the resulting current density vs. voltage curves are shown in **Figure 4**. The halide passivated films showed a significant improvement in performance relative to the purely

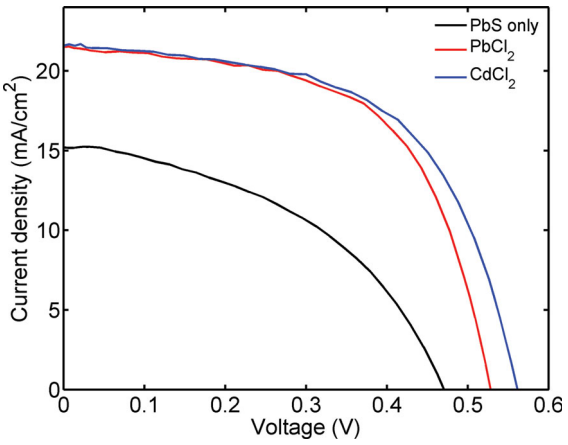

Figure 4. Experimental *J–V* curves of devices under simulated AM1.5G illumination.

organic passivated device. In particular, the reduction in subgap states results in an improved V_{OC}, with the $CdCl_2$ passivated sample demonstrating the largest voltage at open-circuit conditions. Transport is improved due to the enhanced mobility and the increased lifetime as a result of better passivation.[5] The improvements in the charge transport are also manifested in the improved current extraction from the halide passivated devices.

In summary, we used photoelectron spectroscopy to map the full electronic structure of PbS CQD films and observed the effects of different passivation strategies on device-relevant states in the vicinity of the bandgap. We found that halide passivated films have a drastic reduction in states in the midgap as measured both by PES and IPES, which contributes to the improvements in device performance. Interestingly, a reduction is also seen in conduction band tail states when using $CdCl_2$ instead of $PbCl_2$, confirming the role of the bond adaptability of surface cations in preventing shallow trap formation. Short-circuit-current transient spectroscopy confirmed that charge transport is improved in halide passivated films, and device studies demonstrated the benefits to the photovoltaic performance. This study provides a platform for investigating the electronic structure of CQD films, including direct evidence for the formation of detrimental deep and shallow trap states, as well as motivation for reducing their density. Further progress in advancing CQD photovoltaic performance will involve careful surface management to avoid these trap states, potentially through identification of better ligand materials or even passivating shells which have helped in light-emission applications, but have thus far limited carrier transport in photovoltaic applications. Combining the tools demonstrated here with rational materials design will be key for developing efficient, low cost solution processed solar cells.

Experimental Section

Quantum Dot Film Preparation: For PES measurements, quantum dot films were prepared in an ambient atmosphere on indium tin oxide

(ITO)-coated glass substrates in a layer-by-layer approach, similar to those used in previous reports of CQD solar cells.[4,26] Briefly, an octane solution of CQDs (with or without metal halide passivation according to previous reports[4]) was spin-cast onto the substrate (2500 rpm, 1000 rpm s^{-1} acceleration, 10 s). A solution of 1% v/v MPA in methanol was used to perform the solid-state exchange, followed by rinsing with pure methanol. This process was repeated four times to build a pinhole-free film thick enough (ca. 100 nm) to eliminate any contribution from the underlying substrate.

Photoelectron Spectroscopy Measurements: The IPES spectra were obtained by using incident electrons with varying kinetic energy while detecting the emitted photons at a fixed energy (9.7 eV) using a Geiger–Müller detector. The inverse photoemission spectroscopy resolution was limited by an instrumental linewidth of approximately 400 meV. The PES studies were carried out at the photoemission endstation of the PGM beamline at the Canadian Light Source, Inc., equipped with a Scienta SES100 hemispherical electron energy analyzer with a total energy resolution of 50 meV. All the spectra were collected at normal emission and room temperature.

Quantum Dot Device Fabrication: For photocurrent transient and photovoltaic measurements, CQD films were prepared as above but on TiO_2 electrodes on fluorine-doped tin oxide (FTO)-coated glass (TEC15, Hartford Glass) and to a total film thickness of ca. 300 nm (10 layers). To form the electrodes, an aqueous solution of ZnO nanoparticles (NanoShield ZN-2000, diluted to 20% in deionized water) was spin-cast (2500 rpm for 20 s) on the substrates and put on a 150 °C hotplate for 30 min. The substrates were then immersed in a 120 mm $TiCl_4$ solution and placed for 30 min in an oven that was held at 70 °C. The substrates were then dried and annealed on a hotplate at 520 °C for half an hour.

Photocurrent Transient Measurements: A pulsed 640 nm diode laser was used to excite photocarriers in the device. The light intensity was set to approximately 1 sun (100 mW cm^{-2}). Photocurrent characteristics were measured as a function of bias and the effective transit times (defined as the time required for current to decay to $1/e$ of the peak value) were calculated. The mobility was extracted by comparing the transit time as a function of the average field. All the measurements were performed under N_2 flow.

Photovoltaic Device Measurements: Current–voltage characteristics were measured under N_2 flow using a Keithley 2400 source meter with 100 mW cm^{-2} simulated AM1.5 solar illumination (Sciencetech, Class A). The source intensity was measured using a Melles–Griot broadband power meter through a 0.049 cm^2 circular aperture. The estimated uncertainty of the measurements is ±7%.

Density Functional Theory Calculations: DFT simulations were performed following the methodology outlined in our previous work.[8] Briefly, SIESTA software[38] was used with an atomic orbitals basis set of double-zeta plus polarization quality and norm-conserving Troullier–Martins pseudopotentials with non-linear core corrections. A charge-density-grid cutoff of 300 Ry was used. A Pb-rich CQD of 2.4 nm size (ca. 400 atoms in the core) with similar amounts of Cl and MPA ligands was constructed and fully relaxed. The total amount of ligands was adjusted to exactly compensate the excess of Pb, to achieve an undoped structure.[32]

Acknowledgements

This publication is based in part on work supported by Award KUS-11-009-21 made by King Abdullah University of Science and Technology (KAUST), by the Ontario Research Fund Research Excellence Program, and by the Natural Sciences and Engineering Research Council (NSERC) of Canada. The authors acknowledge the help of Dr. C. Y. Kim, K. W. Kemp, and D. Kopilovic. Computations were performed on the TCS supercomputer at the SciNet HPC Consortium. SciNet is funded by the Canada Foundation for Innovation under the auspices of Compute Canada, the Government of Ontario, the Ontario Research Fund – Research Excellence, and the University of Toronto.[39] Research described in this paper was performed at the Canadian Light Source, which is funded by the Canada Foundation for Innovation, the Natural Sciences and Engineering Research Council of Canada, the National Research Council Canada, the Canadian Institutes of Health Research, the Government of Saskatchewan, Western Economic Diversification Canada, and the University of Saskatchewan.

Received: August 19, 2013
Revised: September 30, 2013
Published online: November 15, 2013

[1] E. H. Sargent, *Nat. Photonics* **2012**, *6*, 133–135.
[2] P. V. Kamat, *J. Phys. Chem. Lett.* **2013**, *4*, 908–918.
[3] X. Wang, G. I. Koleilat, J. Tang, H. Liu, I. J. Kramer, R. Debnath, L. Brzozowski, D. A. R. Barkhouse, L. Levina, S. Hoogland, E. H. Sargent, *Nat. Photonics* **2011**, *5*, 480–484.
[4] A. H. Ip, S. M. Thon, S. Hoogland, O. Voznyy, D. Zhitomirsky, R. Debnath, L. Levina, L. R. Rollny, G. H. Carey, A. Fischer, K. W. Kemp, I. J. Kramer, Z. Ning, A. J. Labelle, K. W. Chou, A. Amassian, E. H. Sargent, *Nat. Nanotechnol.* **2012**, *7*, 577–582.
[5] D. Zhitomirsky, O. Voznyy, S. Hoogland, E. H. Sargent, *ACS Nano* **2013**, *7*, 5282–5290.
[6] P. Nagpal, V. I. Klimov, *Nat. Commun.* **2011**, *2*, 486.
[7] Y. Gao, M. Aerts, C. S. S. Sandeep, E. Talgorn, T. J. Savenije, S. Kinge, L. D. A. Siebbeles, A. J. Houtepen, *ACS Nano* **2012**, *6*, 9606–9614.
[8] O. Voznyy, S. M. Thon, A. H. Ip, E. H. Sargent, *J. Phys. Chem. Lett.* **2013**, *4*, 987–992.
[9] P. Stadler, B. R. Sutherland, Y. Ren, Z. Ning, A. Simchi, S. M. Thon, S. Hoogland, E. H. Sargent, *ACS Nano* **2013***7*, 5757–5762.
[10] D. Bozyigit, M. Jakob, O. Yarema, V. Wood, *ACS Appl. Mater. Interfaces* **2013**, *5*, 2915–2919.
[11] S. M. Thon, A. H. Ip, O. Voznyy, L. Levina, K. W. Kemp, G. H. Carey, S. Masala, E. H. Sargent, *ACS Nano* **2013**, *7*, 7680–7688.
[12] K. S. Jeong, J. Tang, H. Liu, J. Kim, A. W. Schaefer, K. Kemp, L. Levina, X. Wang, S. Hoogland, R. Debnath, L. Brzozowski, E. H. Sargent, J. B. Asbury, *ACS Nano* **2012**, *6*, 89–99.
[13] J. Zhang, X. Jiang, *J. Phys. Chem. B* **2008**, *112*, 9557–9560.
[14] M. Valden, X. Lai, D. W. Goodman, *Science* **1998**, *281*, 1647–1650.
[15] K. Katsiev, B. Yildiz, K. Balasubramaniam, P. A. Salvador, *Appl. Phys. Lett.* **2009**, *95*, 092106–092106–3.
[16] I. Swart, Z. Sun, D. Vanmaekelbergh, P. Liljeroth, *Nano Lett.* **2010**, *10*, 1931–1935.
[17] B. Diaconescu, L. A. Padilha, P. Nagpal, B. S. Swartzentruber, V. I. Klimov, *Phys. Rev. Lett.* **2013**, *110*, 127406.
[18] W. Xiong, D. D. Hickstein, K. J. Schnitzenbaumer, J. L. Ellis, B. B. Palm, K. E. Keister, C. Ding, L. Miaja-Avila, G. Dukovic, J. L. Jimenez, M. M. Murnane, H. C. Kapteyn, *Nano Lett.* **2013**, *13*, 2924–2930.
[19] K. Overgaag, P. Liljeroth, B. Grandidier, D. Vanmaekelbergh, *ACS Nano* **2008**, *2*, 600–606.
[20] M.-C. Shih, B.-C. Huang, C.-C. Lin, S.-S. Li, H.-A. Chen, Y.-P. Chiu, C.-W. Chen, *Nano Lett.* **2013**, *13*, 2387–2392.
[21] Z.-L. Guan, J. B. Kim, H. Wang, C. Jaye, D. A. Fischer, Y.-L. Loo, A. Kahn, *Org. Electron.* **2010**, *11*, 1779–1785.
[22] M. Bär, S. Pookpanratana, L. Weinhardt, R. G. Wilks, B. A. Schubert, B. Marsen, T. Unold, M. Blum, S. Krause, Y. Zhang, A. Ranasinghe, K. Ramanathan, I. Repins, M. A. Contreras, S. Nishiwaki, X. Liu, N. R. Paudel, O. Fuchs, T. P. Niesen, W. Yang, F. Karg, A. D. Compaan, W. N. Shafarman, R. Noufi, H.-W. Schock, C. Heske, *J. Electron Spectrosc. Relat. Phenom.* **2012**, DOI 10.1016/j.elspec.2012.10.004.
[23] J. Meyer, R. Khalandovsky, P. Görrn, A. Kahn, *Adv. Mater.* **2011**, *23*, 70–73.
[24] K. Kanai, K. Koizumi, S. Ouchi, Y. Tsukamoto, K. Sakanoue, Y. Ouchi, K. Seki, *Org. Electron.* **2010**, *11*, 188–194.

[25] N. F. Mott, *Proc. Phys. Soc. Sect.* **1949**, *62*, 416.
[26] D. A. R. Barkhouse, R. Debnath, I. J. Kramer, D. Zhitomirsky, A. G. Pattantyus-Abraham, L. Levina, L. Etgar, M. Grätzel, E. H. Sargent, *Adv. Mater.* **2011**, *23*, 3134–3138.
[27] R. Böttner, S. Ratz, N. Schroeder, S. Marquardt, U. Gerhardt, R. Gaska, J. Vaitkus, *Phys. Rev. B* **1996**, *53*, 10336–10343.
[28] T. Ollonqvist, T. Kaurila, M. Isokallio, M. Punkkinen, J. Väyrynen, *J. Electron Spectrosc. Relat. Phenom.* **1995**, *76*, 729–734.
[29] S. J. O. Hardman, D. M. Graham, S. K. Stubbs, B. F. Spencer, E. A. Seddon, H.-T. Fung, S. Gardonio, F. Sirotti, M. G. Silly, J. Akhtar, P. O'Brien, D. J. Binks, W. R. Flavell, *Phys. Chem. Chem. Phys.* **2011**, *13*, 20275–20283.
[30] J. Akhtar, M. A. Malik, P. O'Brien, K. G. U. Wijayantha, R. Dharmadasa, S. J. O. Hardman, D. M. Graham, B. F. Spencer, S. K. Stubbs, W. R. Flavell, D. J. Binks, F. Sirotti, M. E. Kazzi, M. Silly, *J. Mater. Chem.* **2010**, *20*, 2336–2344.
[31] W. K. Bae, J. Joo, L. A. Padilha, J. Won, D. C. Lee, Q. Lin, W. Koh, H. Luo, V. I. Klimov, J. M. Pietryga, *J. Am. Chem. Soc.* **2012**, *134*, 20160–20168.
[32] O. Voznyy, D. Zhitomirsky, P. Stadler, Z. Ning, S. Hoogland, E. H. Sargent, *ACS Nano* **2012**, *6*, 8448–8455.
[33] D. Zhitomirsky, M. Furukawa, J. Tang, P. Stadler, S. Hoogland, O. Voznyy, H. Liu, E. H. Sargent, *Adv. Mater.* **2012**, *24*, 6181–6185.
[34] Z. Li, F. Gao, N. C. Greenham, C. R. McNeill, *Adv. Funct. Mater.* **2011**, *21*, 1419–1431.
[35] Y. Liu, M. Gibbs, J. Puthussery, S. Gaik, R. Ihly, H. W. Hillhouse, M. Law, *Nano Lett* **2010**, *10*, 1960–1969.
[36] T. Hanrath, J. J. Choi, D.-M. Smilgies, *ACS Nano* **2009**, *3*, 2975–2988.
[37] A. T. Heitsch, R. N. Patel, B. W. Goodfellow, D.-M. Smilgies, B. A. Korgel, *J Phys Chem C* **2010**, *114*, 14427–14432.
[38] J. M. Soler, E. Artacho, J. D. Gale, A. García, J. Junquera, P. Ordejón, D. Sánchez-Portal, *J. Phys. Condens. Matter* **2002**, *14*, 2745–2779.
[39] C. Loken, D. Gruner, L. Groer, R. Peltier, N. Bunn, M. Craig, T. Henriques, J. Dempsey, C.-H. Yu, J. Chen, L. J. Dursi, J. Chong, S. Northrup, J. Pinto, N. Knecht, R. V. Zon, *J. Phys. Conf. Ser.* **2010**, *256*, 012026.